IEEE Photonics Journal
An IEEE Photonics Society Publication

Characterization of Optical Coherence Tomography Images Acquired at Large Distances With Large-Diameter Beams

Volume 6, Number 3, June 2014

Dan P. Popescu
Michael S. D. Smith
Michael G. Sowa

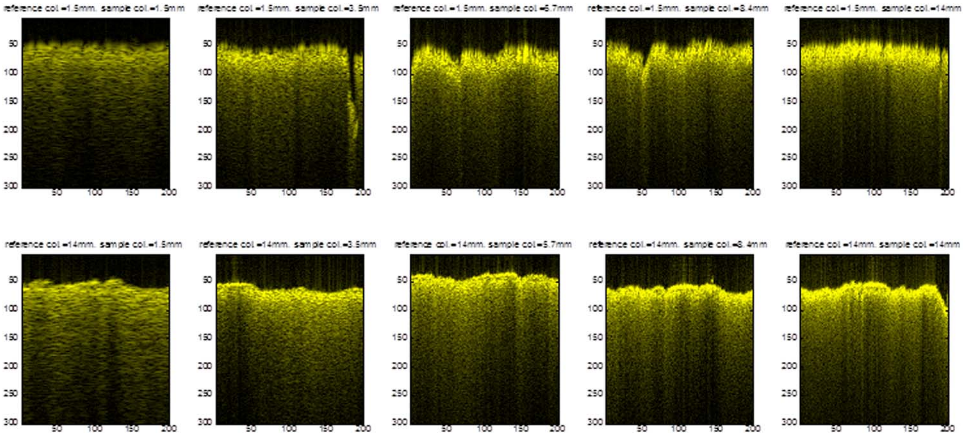

DOI: 10.1109/JPHOT.2014.2321754

Characterization of Optical Coherence Tomography Images Acquired at Large Distances With Large-Diameter Beams

Dan P. Popescu, Michael S. D. Smith, and Michael G. Sowa

Medical Devices Portfolio, National Research Council of Canada, Winnipeg, MB R3B 1Y6, Canada

DOI: 10.1109/JPHOT.2014.2321754

Manuscript received March 21, 2014; revised April 23, 2014; accepted April 25, 2014. Date of current version May 14, 2014. This work was supported by the Chemical, Biological, Radiological, Nuclear, and Explosive (CBRNE) Research and Technology Initiative (CRTI) within the Canadian Safety and Security Program (CSSP), under Project 30vx00 (previously CRTI 09-481TD): An Optical Imaging Device for a Rapid Assessment of Tissue Viability and Wound Healing. Corresponding author: P. Dan (e-mail: dan.popescu@nrc-cnrc.gc.ca).

Abstract: We tested the imaging capabilities for variants of a 1550-nm swept-source fiber-based optical coherence tomography system with a telecentric system incorporated at the end of its sample arm. The system was designed for *in vivo* imaging of burns; therefore, we acquired images from samples located at distances greater than 24 cm from the exit of the telecentric system. Each system variation had a specific combination of diameters for the reference and sample beams. In the reference arm, we used, alternately, two collimated beams with diameters of 1.5 and 14 mm, respectively. In the sample arm, we tested collimated beams with the following diameters: 1.5, 3.5, 5.7, 8.4, and 14 mm. A galvanometric mirror system scanned the collimated sample beam across the entrance pupil of the telecentric system. The sample beam exited the telecentric system parallel with its optical axis and convergent onto the sample. Depending on the collimator used in the sample arm, images were acquired with beams focused to waist diameters ranging from 40 to 240 μm. We acquired images with the sample at different locations within a $\pm$30 mm range centered about the sample beam waist. Furthermore, we used the signal-to-noise ratio, the detected signal intensity, and the visual appearance to compare images acquired with different sample/reference beam configurations.

Index Terms: Optical coherence tomography, medical optics instrumentation, image analysis, speckle.

1. Introduction

In the last two decades, optical coherence tomography (OCT) has become widely used in industrial and biomedical applications. During this period, various aspects of OCT instrumentation achieved considerable technical refinements but efforts were almost exclusively focused on obtaining probing beams with the smallest waist diameter allowed by particular OCT configurations. There is indeed a general agreement that a smaller probing diameter increases the transversal resolution and enhances the intensity of the detected OCT signal. As a result of this consensus OCT systems generally employ probing beams with waist diameters smaller than 15 μm. Consequently, investigation of images generated with weakly-focused large-diameter sample beams has been a neglected area of OCT imaging. At this point, there is only one study reporting image acquisition using a probe beam with a diameter of 180 μm at a working distance of 4 cm [1]. In addition, there are also very few reports that directly compare OCT images obtained with probing beams of different diameters. The one publication that reports such work compares OCT images acquired with beams of different diameters, but all smaller than 12 μm [2].

Nevertheless, acquisition of OCT images with weakly focused beams is a direction worth pursuing. Basic beam propagation theory suggests at least two distinct advantages. Firstly, the Rayleigh lengths could have values in the centimeter range. Such values would assure an almost constant illumination over the entire depth probed when imaging a light scattering sample. In these cases the probed depth usually extends over a 0.2–2 mm range. Secondly, even more important, beams focused to large-diameter waists ensure a larger stand-off distance between sample and the optical components from the end of the sample arm. The capability to acquire OCT images from samples located further away from the probing head can be a very important and critical parameter for some *in vivo* and industrial OCT applications [3]. For example, we are developing the OCT platform investigated in this study with the purpose of acquiring *in vivo* images of burnt skin from patients in hospital settings. Burn injuries are notoriously prone to infections so larger distances between lesion and surrounding instruments prevent possible contaminations. For the subsequent clinical imaging stage, we aim for a minimum distance of 24 cm. We also designed the system to acquire OCT images across a maximum surface of 8 cm × 8 cm in one-second long acquisition cycles in order to minimize the effects induced in OCT data by patient's respiratory movements.

2. Experimental Setup

A swept-source optical fiber-based OCT platform was used to acquire the data presented in this work. The OCT platform was built using Clear Curve single mode Corning optical fibers. The swept laser source (HSL-series, Santec) had a central wavelength of 1545 nm and a 140 nm spectral range measured at half the maximum intensity. The average output power of the swept source is 14 mW and the coherence length of the swept laser line is 11 mm. The free-space axial resolution of this system, measured at the full-width half-maximum (FWHM) of the source autocorrelation function, is 12 μm. The light source has a repetition rate of 20 kHz and a duty cycle of 85%. The maximum imaging depth is 11 mm with a -20 dB signal roll-off at the 4.5 mm depth. The light output from the swept source was launched into a 2 × 2 coupler, with 90% of the available power directed toward the sample arm, and 10% guided into the reference arm. Both arms contain circulators to guide the light back-reflected from the sample and from the reference mirror toward a balanced 2 × 2 coupler and the subsequent detector. The detection was performed with a 75 MHz bandwidth dual-channel balanced amplified photodetector (PDB 120C, Thorlabs). The detector output was digitized using a data acquisition card (ATS9462, AlazarTech) with 16-bit resolution and a sampling speed of 100 MS/s. In the acquired OCT images, the pixel sampling axial distance is 6.25 μm. A diagram of the OCT platform is displayed in Fig. 1.

As detailed in the diagram, the reference arm of the interferometer was terminated with an optical fiber collimator and a fixed flat mirror. The back-reflected beam was still collimated when returned to the reference collimator. Two collimator types were used alternately in the reference arm; one outputs a beam with a diameter of 1.5 mm while the other outputs a 14-mm diameter beam. Similarly, we used various collimators in the sample arm outputting beams with the following diameters: 1.5 mm, 3.5 mm, 5.7 mm, 8.4 mm and 14 mm. All collimators used in this study were pigtail style and were acquired from Oz Optics. We measured all beam diameters used in this application to $1/e^2$ of the intensity. In the sample arm, upon exiting the collimator, the beam encountered a galvanometric system (6240HM, Cambridge Technology) with two mirrors that scanned the beam across the entrance of a telecentric f-theta lens system (TSL-1550-80-195-Ronar-Smith) with an angular amplitude of $\pm 12^\circ$. The galvanometric system had its fulcrum located at a free-space total distance of 5 cm from the entrance of the telecentric system. Based on the measured beam waists and waist locations, the values for the effective numerical apertures (NA) of sample beams after they exited the corresponding collimators and passed through the telecentric system were as follows: 0.0038, 0.0089, 0.0146, 0.0205 and 0.0359, respectively. With a

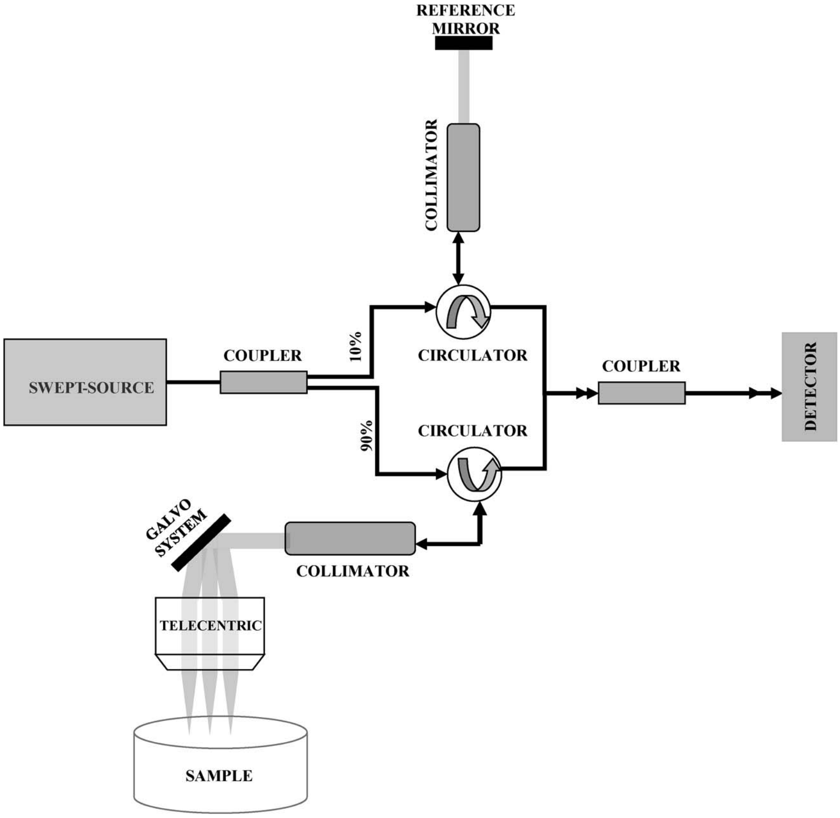

Fig. 1. The diagram of the OCT platform. A telecentric system was integrated into the sample arm. Probing beam exits the telecentric system convergent and parallel to its optical axis. All images were acquired with sample at distances greater than 24 cm from the exit of the telecentric system.

manufacturer-recommended working distance of 272 mm in the image plane for a 15-mm diameter collimated beam entering the system, the telecentric system kept the probing beam parallel to its main optical axis while scanning it across a maximum field of view of 8 cm $\times$ 8 cm.

The swept source provided the trigger signal that initiated the acquisition sequence for an OCT depth line (or A-scan). A reference “k-clock” signal was used to resample the data acquired through the DAQ so it became linear with respect to the optical wave-number. A-scans were then obtained through a discreet Fourier transform of the resampled data. The swept source trigger signal was also used to synchronize the motion of the galvanometric scanner. In-house programmed LabView software was used for data acquisition via a DAQ card and for controlling the galvanometric scanner via a multi-purpose I/O card (USB-6341, National Instruments).

A 0.75-mm thick layer of cork located on the back of a metallic ruler was used as sample. We selected this sample because it provides defined surface and subsurface structures for visualization in OCT images. Also, its configuration does not change with time. Configuration-wise, when investigated with an optical microscope, the sample looks like a conglomerate of smaller structures, each with a surface width of about 100 μm, value greater than the distance between adjacent a-scans but comparable with the diameters of probing beams. Sample positioning was carefully monitored so that OCT images were acquired from approximately the same location on the surface. Based on observed surface homogeneity, despite the fact that co-location from image to image was not perfect, direct comparisons between OCT images acquired with different system configurations were possible. All OCT images were recorded near the zero-delay point, with the length of the reference arm modified accordingly to match the length of the sample arm after each sample displacement.

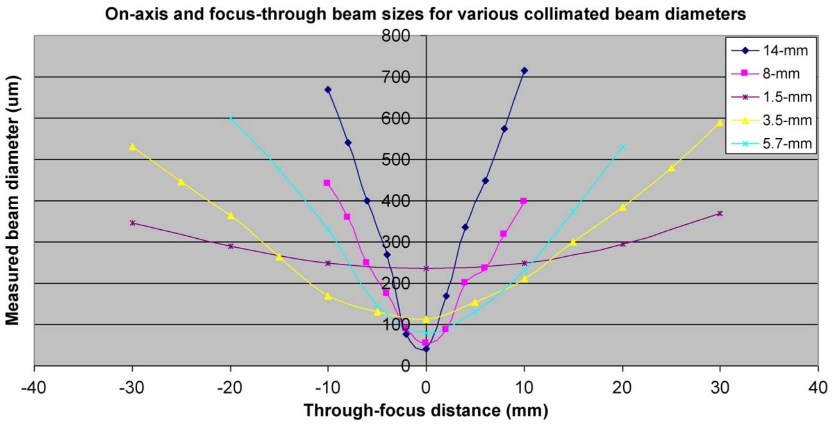

Fig. 2. Beam diameters are measured along the optical axis about the waist location for each sample collimator. Negative distances represent locations closer to the telecentric system while positive distances represent locations that are further away.

3. Measurements and Results

As a preliminary step, we investigated the beams in the sample arm after they propagated through the telecentric system. During this step, we determined the waist locations, the waist diameters, as well as the beam diameters at locations along the telecentric optical axis within a ±30 mm range centered about the waist positions. This range helped us to quantify the effects induced on image quality by breathing motion. All diameters were measured at $1/e^2$ from the maximum power using a Spiricon SP90001-LBA-FW-SCOR-20 beam profiler and with the reference arm blocked. The waist values measured along the main axis of the telecentric system were 40 μm, 55 μm, 80 μm, 115 μm, and 240 μm corresponding to the following collimated diameters: 14 mm, 8.4 mm, 5.7 mm, 3.5 mm and 1.5 mm, respectively. For the same sequence of diameters, the following telecentric confocal depths, defined as the distance between the locations where beam diameter became twice the waist, resulted from these intensity measurements: 4 mm, 6 mm, 15 mm, 25 mm and 70 mm, respectively. Fig. 2 displays the beam diameters measured along the telecentric optical axis.

To verify diameter consistency across the area of interest, we also measured the diameters for beams exiting the telecentric system after they entered at 6° and 12° with respect to its main optical axis. The telecentric system role was to transform a collimated beam entering at an angle with respect to its main optical axis into an exiting convergent beam that propagates parallel to the main axis. The distance between the propagation direction of exiting beam and the main optical axis was proportional to the angle between the entering collimated beam and the main axis. Thus, when entering at 6° and 12° angles the beams exited the telecentric propagating parallel to the main axis but displaced off-axis by 20 mm and 40 mm, respectively. Due to the circular symmetry of the telecentric system, these two cases offered good insight into the beam characteristics across the whole field of view. For each collimator we established that all diameters measured off-axis in planes perpendicular on the main optical axis were consistent, within maximum 7%, with the corresponding on-axis value measured in the same plane. The differences between the off-axis values and the corresponding on-axis ones were smaller than 7% for the 1.5-mm, 3.5-mm and 5.7-mm collimators. In addition, the off-axis beams kept a good circular symmetry with differences between the saggital and tangential diameters being smaller than 10% for all investigated cases. Beam circularity degraded only at the extremes of the investigated axial range (i.e. in planes located at more than ±20 mm from the waist), and of the lateral range (i.e. along the parallel axis 40-mm away from the main optical axis) and, only for the largest diameter collimators (the 8-mm and the 14-mm). In addition to demonstrating the good quality of optical components used for this investigation, these results provide assurance about the consistency of beam diameters used for OCT data acquisition across the scanning range of interest.

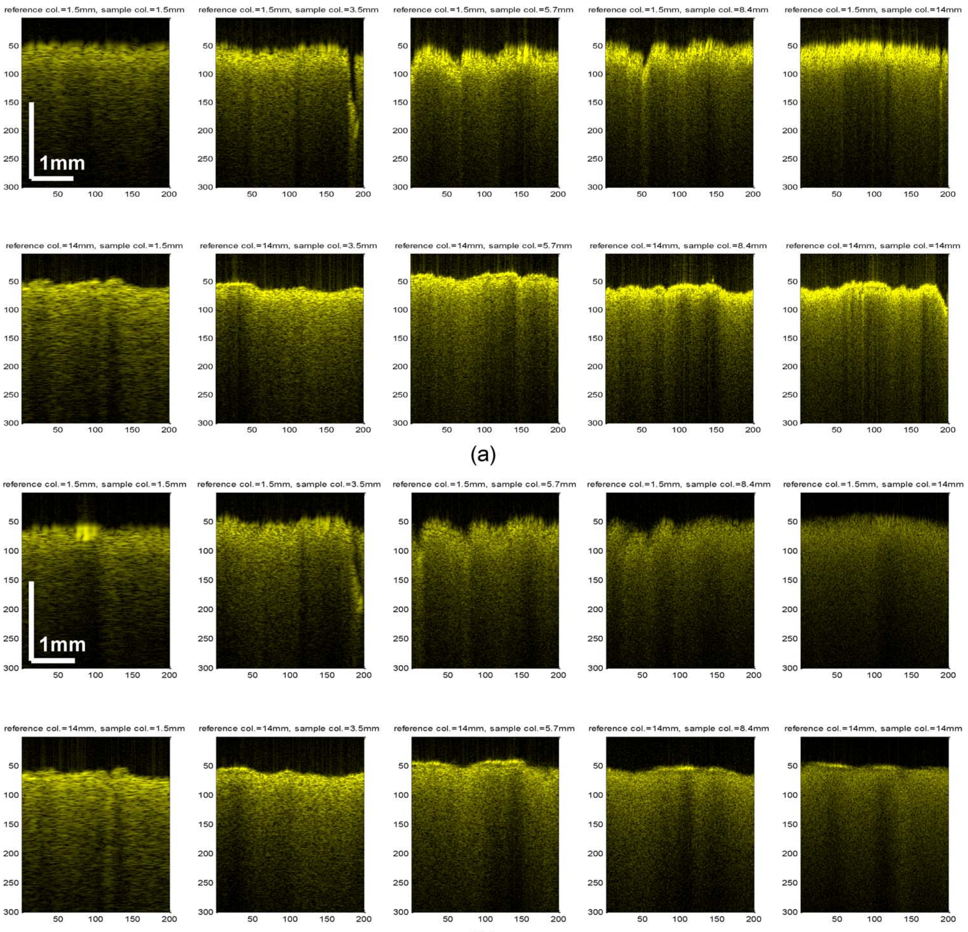

(a)

(b)

Fig. 3. (a) OCT images acquired with collimated sample beams of the following diameters from left to right: 1.5 mm, 3.5 mm, 5.7 mm, 8.4 mm and 14 mm. The beam diameters in the reference arm are 1.5 mm (top) and 14 mm (bottom). For each image, the sample is located in the waist plane where the telecentric system generates the smallest diameter for the probing beam exiting the corresponding collimator. Distance between adjacent depth scans is 20 μm. (b) Same as Fig. 3(a) but sample was located 10 mm further away from the image plane where the telecentric system generates the smallest diameter for a particular collimated sample in the sample arm.

The next stage of our work was to acquire OCT images using different reference/sample beam configurations. We always positioned the sample perpendicular to the telecentric axis. As mentioned, we recorded all images near the zero-delay, with the length of the reference arm balanced accordingly after each sample displacement. This procedure ensured that the sensitivity roll-off performance of the swept-source OCT system was not a factor in the subsequent image analysis.

Fig. 3(a) and (b) shows OCT images of the cork layer acquired with different sample/reference collimator pairs. The images in Fig. 3(a) were acquired with the sample positioned at the waist of the probing beam and perpendicular to the telecentric axis. Meanwhile, the images displayed in Fig. 3(b) were acquired with the sample 10 mm away from the waist plane. In both figures, the top row images were obtained with a 1.5 mm collimator at the end of the reference arm. Meanwhile, images displayed on the bottom rows were acquired with the 14 mm collimator in the reference arm. Each image consists of 200 a-scans with a 20 μm distance between adjacent a-scans.

It is noticeable in Fig. 3(a) that more surface details are distinguishable when the diameter of the collimated beam was larger before entering the telecentric system. This is consistent with the general expectation that transversal resolution increases as the spot size of the probing beam decreases, i.e. from 240 μm (left, top and bottom rows) to $\sim$40 μm (right, top and bottom rows) in Fig. 3(a). Meanwhile, the surface resolution in the images from Fig. 3(b) is degraded when compared to their corresponding images in Fig. 3(a) due to increase of probing beam diameters. The beam diameters measured at the locations where images from Fig. 3(b) were acquired were 250 μm, 210 μm, 230 μm, 400 μm, and 710 μm corresponding to the following collimated diameters: 1.5 mm, 3.5 mm, 5.7 mm, 8.4 mm and 14 mm, respectively. Surface details are also becoming less prominent in Fig. 3(b) for both reference arm configurations as OCT images are inspected from left to right. Due to beam divergence, the reduction in transversal resolution is obvious especially for images corresponding to configurations which employed the 8.4 and the 14-mm collimators in the sample arm. The transversal resolution degraded even more as we placed the sample even further from the waist plane since the spot size of the probing beam increased at a higher rate for the sample collimators with bigger diameters.

Despite the lower transversal resolution, the speckled pattern appearance is still better in OCT images obtained with the larger diameter collimators in the sample arm due to reduction in the size of coherent speckle. The effect is better noticed when successive images in Fig. 3(a) and (b) are compared starting from the sample collimator with the smallest diameter (smallest NA) to the configuration sporting the largest sample arm collimator (largest NA). Along this sequence, the speckle size is connected to the average coherent speckle sampling, which in turn is determined by the NA. A larger NA contributes to a larger angular spectrum in the coherent transfer function of the OCT system. This in turn results into a smaller FWHM of the autocorrelation function along directions transverse to the optical axis, which is itself proportional to the average transverse size of speckle [4]. Therefore, when the sample was displaced from the telecentric focus, the average speckle size did not change much with sample displacement for the probing beams with small NAs. Indeed, what still changes and degrades in the off-focus cases is the transverse optical resolution, i.e., the ability to resolve distinct surface features, due to the increase of probing beam diameter.

In addition to previous observations, the type of collimator used in the reference arm also plays a role in the visual aspect of OCT images. By comparing images from the top row with the ones in the bottom row in both Fig. 3(a) and (b), an observer can notice that the visual quality of images generated with the 14-mm reference beam is superior to the corresponding images obtained by using the 1.5-mm-diameter one. The dependence of OCT image quality on the reference arm configuration is another subject that has not been extensively investigated. One paper studying such dependence reports a change in the signal-to-noise ration (SNR) but for a different coherent imaging configuration—i.e. a common-path fiber-based Fizeau interferometer [5]. Limited to investigating the effect of reference arm reflectivity and examining non-scattering samples only, the work presented in Ref. [5] reports that SNR improves, up to a saturation value, when the reflectivity in the reference arm increases. Extrapolation of results from Ref. [5] to highly scattering samples, such as the one used for this work, is not straightforward and it should be undertaken with a solid degree of caution [6].

The visual improvement obtained when using the 14-mm collimated beam in the reference arm could be also attributable to reduction in the speckle size, here also the result of reduction in the FWHM of the transverse autocorrelation function [4]. Coherent speckle arises in many contexts where interference is the principle behind the imaging method. OCT images of highly scattering samples are always plagued with a speckled appearance generated by interference between (group delay matched) back-reflected reference wavefronts and single or multiple backscattered sample wavefronts from multiple sample locations lying within the probed resolution (i.e. coherence) volume [2], [7]. There is a vast body of published work dedicated to procedures for decreasing the coherent speckle in OCT images. At their fundamental core, reduction procedures are based on un-correlating phases of propagating optical wavefronts, thus reducing their coherence. After interference, each wavefront generates its own independent speckle and by summation (averaging) of several wavefronts the random coherent noise component decreases leading to improved image. One method to generate uncorrelated wavefronts uses beams with diverse polarizations [8], [9]. Another method involves imaging samples with spatially diverse beams. Variants of this method include angle diversity (illuminate the sample with beams incoming from different directions) [10],

[11], imaging with beams of different frequencies [12], or changing the optical phase of the probing beam through sample displacement [13]. Our OCT configurations provided a degree of angular diversity for the reference beam by expanding it during the transition from the single mode fiber core to the exit of the reference collimator. This effect was repeated during the inverse trip of the backreflected light, delivered back into the lens assemble of the collimator, from there into the fiber core and then sent to interfere with the sample signal. Due to this process we attributed the smaller sized coherent speckle pattern observed in the OCT images acquired with the 14-mm reference beam to a greater angular diversity provided by that collimator's lens assemble then the one obtained by using the 1.5-mm collimator. In the former case, the reference beam expansion to a larger diameter followed by its re-convergence after back-reflection provided an additional boost in angular diversity among the optical wavefronts returning through the reference arm.

Besides visual characterization, we used the maximum signal-to-noise ratio (SNR) and the total intensity of the recorded signal to compare OCT images acquired with different reference/probe beam configurations. To calculate these parameters we first obtained averaged depth profiles from each OCT image by adding fifty consecutive a-scans. Before summation, in order to compensate for surface roughness, the a-scans were aligned along the same horizontal pixel row. Since the distance between adjacent a-scans is 20 μm, their patterns of coherent speckle noise are not highly correlated. Spatial variations on that scale within the sample ensure some degree of pattern decorrelation between adjacent scans. In this case, because of sample-induced spatial diversity, summing successive a-scans greatly also reduces the coherent noise.

While there is a certain degree of correlation between SNR performance and visual quality in OCT images, the size and the contrast of recorded coherent speckle are usually the parameters most correlated to the visual quality of whole OCT images. As previously established, a smaller sized coherent speckle, together with a higher contrast, corresponds to a better developed signal originating from a smaller coherence volume thus resulting into a more detailed representation of the sample and in an overall OCT image carrying a higher amount of visual information. Meanwhile, by adding together multiple a-scans, which have their speckle noise uncorrelated due to inherent spatial diversity (a-scans acquired at different locations) the coherent speckle noise in the resulting averaged profile decreases. Therefore the effect of coherent speckle on the subsequent SNR calculations done on averaged profiles is greatly attenuated compared to its overall effect on the visual appearance of whole OCT images.

The maximum SNR was calculated as the ratio between the peak amplitude and the average of the noise floor in an averaged profile according to the following procedure. First the averaged profile was normalized to unity with respect to its peak amplitude. Then the average noise was determined as the mean intensity of the last one hundred depth pixels of the averaged profile. Finally, a SNR value was obtained by inverting the average noise value. Using the mean value calculated over the last one hundred pixels of an averaged profile ensured that only the signal noise was considered. In our OCT profiles, signal recorded at depths greater than 300 pixels (equivalent to almost 2 mm of optical depth) from the sample surface closely matched the noise signal measured when we recorded light that came only from the reference arm when the sample arm was blocked. This shows that the signal recorded in the tail portions of averaged profiles is shot-noise limited [14]. The second parameter used as a benchmark in this investigation, the signal intensity, was calculated as the summation of signal intensities across a depth range of one hundred and ten depth pixels along the compounded profiles extracted from each acquired OCT image. This range covered about 650 μm of optical depth within the cork layer. For each compounded profile, this range started from the pixel located before the intensity maximum corresponding to the air/cork interface and with its intensity value equal to 50% from that maximum.

Figs. 4 and 5 display the maximum SNR and the OCT signal intensity calculated for various sample/reference beam configurations, and at different distances from the corresponding waist planes. For these calculations we used images acquired consecutively with the sample perpendicular to the telecentric axis and positioned on both sides of the waist and at the following distances: 0 mm, 5 mm, 10 mm, 15 mm, 20 mm, 25 mm and 30 mm. We chose the ±30 mm range because we aim to develop an optimal OCT system for acquiring *in vivo* images of burnt tissue from

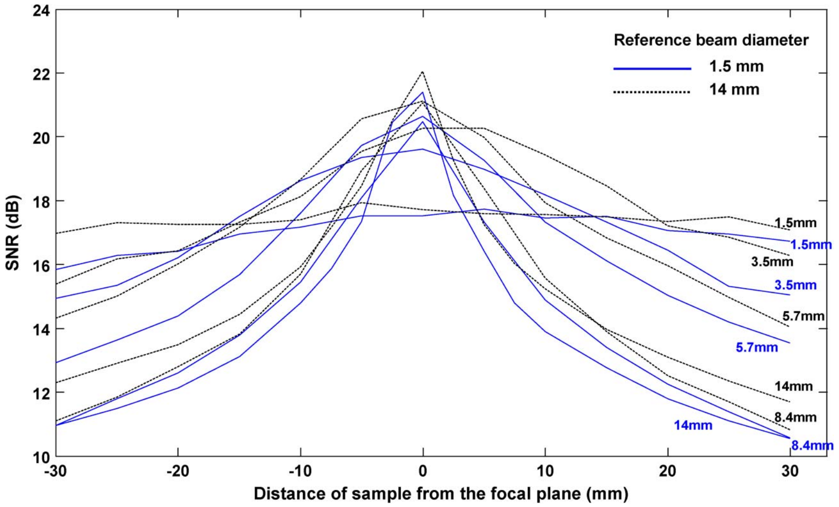

Fig. 4. SNR calculated for multiple sample/reference arm configurations and different distances from the corresponding waist locations. Lines are introduced for a better visualization of trends corresponding to specific collimators. The solid lines correspond to results obtained with the 1.5 mm beam diameter in the reference arm while the dotted ones apply to results generated with the 14 mm reference beam. The diameters of collimators used in the sample arm are listed on the right side of the corresponding profiles.

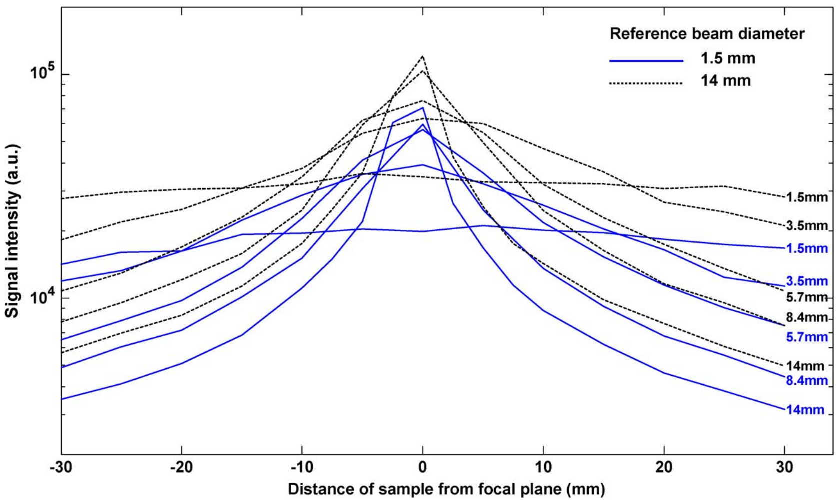

Fig. 5. OCT signal intensity calculated for multiple sample/reference arm configurations and different distances from the corresponding focal planes The solid lines correspond to results obtained with the 1.5 mm beam in the reference arm while the dotted lines apply to results generated with the 14 mm reference beam. The diameters of collimators used in the sample arm are listed on the right side of the corresponding profiles.

regions with respiratory-induced motions within a peak-to-peak amplitude of 60 mm. The abscissa displays distances from the waist, with the negatives marking planes located closer to the telecentric system, while the positives mark locations further away. We listed each diameter of a collimated sample beam before it entered the telecentric system on the right-hand side and close to its corresponding curve. As mentioned, we obtained all SNR and intensity data from images collected near the zero-delay point of each OCT configuration. Through this procedure the intensity roll-off did not become a factor in the subsequent analysis and the probed depth was un-affected by sample displacement.

Each data point in Figs. 4 and 5 represents an average SNR and an average OCT signal intensity, respectively, obtained according to the procedure outlined in this paragraph. Each OCT image was portioned into slices fifty a-scan wide. We obtained an average depth profile from each slice and calculated its corresponding SNR and OCT intensity values. All values calculated for an image acquired at a sample particular location were used to generate the average SNR and OCT signal intensity values displayed in Figs. 4 and 5 at the abscissa points corresponding to the sample axial location. The subsequently calculated standard deviations for the SNR and the OCT signal intensity data points in each image were 1.7% and 2.5%, respectively. The standard deviation values to not modify the trends displayed therefore, to preserve figure clarity, the standard deviation bars have not been included in these figures.

There were several trends common to both SNR values and OCT signal intensities for all investigated OCT configurations. Both parameters attained their maximum values at the waist location and decreased when applied to images acquired from other locations. Both parameters decreased almost symmetrical with distance from the waist position. Regardless of the reference beam diameter, SNR values and OCT intensities decreased more abruptly with distance for configurations employing the sample arm collimators with the largest diameters, 8.4 mm and 14 mm.

The drop in SNR recorded 30 mm away from the maximum value location for configurations with 14-mm and 8.4-mm collimators in the sample arm was approximately 12 dB, while the signal intensities decreased about 1.5 orders of magnitude. The variations in SNR and OCT signal intensity with distance were much smaller for images acquired by using the sample arm collimators with the smaller diameters. Data acquired with the 1.5-mm sample collimator showed almost constant SNR and signal intensity over the investigated range. While the SNR values were almost identical, the 1.5-mm/14-mm probing/reference pair of collimators provided greater OCT signal intensities when compared to the 1.5-mm/1.5-mm pair. In a consistent way this point was also valid for all collimator pairs; i.e. the signal intensity for any configuration with the 14-mm reference beam was greater than its corresponding configuration that had the 1.5-mm diameter reference beam. An explanation for this could be that the amount of signal collected per unit of sample coherent volume better matched the corresponding coherent signal from the reference arm when the 14-mm diameter reference beam was used. When linked to the angular coherence diversity argument previously presented, this fact could also play a role in the better visual quality observed in Fig. 3(a) and (b) for OCT images acquired with the 14-mm diameter reference beam.

For probing beams with collimated diameters greater than 1.5 mm both SNR and OCT signal intensity decreased with distance from the locations of maximum values. Data acquired with the 14-mm and 8.4-mm beam collimators in the sample arm displayed the fastest rates of SNR and signal intensity decreases. As expected, the parameters characterizing configurations with 3.5-mm and 5.7-mm diameter collimators displayed trends intermediary to properties that characterized the 1.5-mm sample arm collimator configuration and to those of the large-diameter group.

The SNR performance of configurations that used 14-mm and 8-mm collimators were quite close over the investigated range of distances. Moreover, their SNR performance was superior to the performance achieved by using the 1.5-mm diameter sample collimator when the sample was located within a ±7 mm distance range centered about the waist location. This was also true for configurations that used the intermediate collimators, i.e. the 3.5-mm and 5.7-mm, but in these cases the region with higher SNR extended over a width centered about the beam waist slightly larger than 30 mm.

The general trends exhibited by the SNR parameter also held for results concerning the OCT signal intensity displayed in Fig. 5. Different divergences induced by the telecentric system on collimated beams of various diameters resulted in different attenuation rates for OCT signal recorded when sample changed locations. The 14-mm reference beam also ensured higher OCT intensities when compared to corresponding configurations that employed the 1.5-mm diameter reference beam. Even in cases when the OCT signal intensities were lower because of higher beam divergences, the OCT configurations with bigger diameter collimators in the sample arm provided images with smaller speckle than displayed in images generated by the configurations with the 1.5-mm sample arm collimator. This property should be exploited with a certain degree of caution due to the inverse correlation between beam divergence and transversal resolution.

4. Conclusion

In this study we used a 1550-nm swept-source fiber-based OCT platform with a telecentric system at the end of the sample arm. We tested ten variants of this OCT platform. Images were acquired by using probing beams focused to five different waists. Each probing beam case was also tested for two diameters of the collimated reference beam: 1.5 mm and 14 mm. OCT images were recorded with the sample displaced within a ±30-mm range centered about the waist of each probing beam. Regardless of sample location, all images were acquired near the zero-delay point of the interferometer. Data analysis was based on the visual appearance of whole OCT images, as well as on the SNR and intensity values calculated from averaged depth profiles. The results are useful to select the OCT configuration most suitable to a specific application. For each OCT system with a specific probing beam, the images collected with the configuration employing the 14-mm-diameter reference beam displayed reductions in speckle size when compared to speckle from images acquired using the 1.5-mm-diameter reference beam. Therefore configurations with the 14-mm-diameter reference beam could be used to resolve smaller coherent volumes within a sample thus providing better spatial resolution. Meanwhile, OCT configurations with the 1.5-mm collimator in the sample arm displayed almost constant SNR and signal intensity within the probed range of sample displacement, making them suitable for imaging samples in oscillatory motion about the waist plane or stationary samples positioned off that plane. Meanwhile, there is a 15-mm wide region, centered about the waist position, where SNR was higher when the collimators with diameters of 8.4 mm and 14 mm were used in the sample arm compared to SNR obtained by using the 1.5-mm sample collimator. These configurations can be optimal for the following situations: static sample positioned at or near the waist plane, or sample in small-amplitude motion about the waist plane, or sample in any type of oscillation about the waist plane but with the OCT image acquisition triggered when sample passes through the higher SNR region. We also concluded that the configuration with a 14-mm collimated reference beam and with an 8.4-mm collimated beam passing through the telecentric system in the sample arm is optimal for *in vivo* assessing of large-area burns. The previous observations are also true for configurations incorporating sample arm collimators with diameters of 3.5 mm and 5.7 mm. Their maximum SNR values are lower than the values corresponding to configurations with larger sample beam diameters, but the region with higher SNR than the values calculated for the 1.5-mm case extends almost 30 mm. With few exceptions, the intensity of recorded OCT signal shows a quite similar behavior with the one displayed by SNR.

References

[1] J. Armstrong *et al.,* "*In vivo* size and shape measurement of the human upper airway using endoscopic long range optical coherence tomography," *Opt. Exp.*, vol. 11, no. 15, pp. 1817–1826, Jul. 2003.

[2] J. M. Schmitt, A. Knüttel, M. Yadlovski, and M. A. Eckhaus, "Optical coherence tomography of a dense tissue: Statistics of attenuation and backscattering," *Phys. Med. Biol.*, vol. 39, no. 10, pp. 1705–1720, Oct. 1994.

[3] I. Grulkowski *et al.,* "High-precision, high-accuracy ultralong-range swept-source optical coherence tomography using vertical cavity surface emitting laser light source," *Opt. Lett.*, vol. 38, no. 5, pp. 673–675, Mar. 2013.

[4] A. Curatolo, B. F. Kennedy, D. D. Sampson, and T. R. Hillman, "Speckle in optical coherence tomography," in *Advanced Biophotonics*, R. K. Wang and V. V. Tuchin, Eds. New York, NY, USA: Taylor & Francis, 2013, pp. 211–277.

[5] X. Li, J.-H. Han, X. Liu, and J. U. Kang, "Signal-to-noise ratio analysis of all-fiber common-path optical coherence tomography," *Appl. Opt. vol.*, vol. 47, no. 27, pp. 4833–4840, Sep. 2008.

[6] A. G. Podoleanu, "Unbalanced versus balanced operation in an optical coherence tomography system," *Appl. Opt.*, vol. 39, no. 1, pp. 173–182, Jan. 2000.

[7] J. M. Schmitt, S. H. Xiang and, and K. M. Yung, "Speckle in optical coherence tomography," *J. Biomed. Opt.*, vol. 4, no. 1, pp. 95–105, Jan. 1999.

[8] J. W. Goodman, *Laser Speckle and Related Phenomena*, J. C. Dainty, Ed. Berlin, Germany: Springer-Verlag, 1984, pp. 142–186.

[9] M. Kobayashi, H. Hanafusa, K. Takada, and J. Noda, "Polarization-independent interferometric optical-time-domain reflectometer," *J. Lightw. Technol.*, vol. 9, no. 5, pp. 623–628, May 1991.

[10] J. M. Schmitt, "Array detection for speckle reduction in optical coherence microscopy," *Phys. Med. Biol.*, vol. 42, no. 7, pp. 1427–1440, Jul. 1997.

[11] M. Bashkansky and J. Reintjes, "Statistics and reduction of speckle in optical coherence tomography," *Opt. Lett.*, vol. 25, no. 8, pp. 545–547, Apr. 2000.
[12] M. Pircher, E. Gotzinger, R. Leitgeb, A. F. Fercher, and C. K. Hitzenberger, "Speckle reduction in optical coherence tomography by frequency compounding," *J. Biomed. Opt.*, vol. 8, no. 3, pp. 565–569, Jul. 2003.
[13] D. P. Popescu, M. Hewko, and M. G. Sowa, "Speckle noise attenuation in optical coherence tomography by compounding images acquired at different positions of the sample," *Opt. Commun.*, vol. 269, no. 1, pp. 247–251, Jan. 2007.
[14] N. Nassif *et al.,* "*In vivo* human retinal imaging by ultrahigh-speed spectral domain optical coherence tomography," *Opt. Lett.*, vol. 29, no. 5, pp. 480–482, Mar. 2004.